

Alignment of an interferometric gravitational wave detector

Peter Fritschel, Nergis Mavalvala, David Shoemaker, Daniel Sigg, Michael Zucker, and Gabriela González

Interferometric gravitational wave detectors are designed to detect small perturbations in the relative lengths of their kilometer-scale arms that are induced by passing gravitational radiation. An analysis of the effects of imperfect optical alignment on the strain sensitivity of such an interferometer shows that to achieve maximum strain sensitivity at the Laser Interferometer Gravitational Wave Observatory requires that the angular orientations of the optics be within 10^{-8} rad rms of the optical axis, and the beam must be kept centered on the mirrors within 1 mm. In addition, fluctuations in the input laser beam direction must be less than 1.5×10^{-14} rad/ $\sqrt{\text{Hz}}$ in angle and less than 2.8×10^{-10} m/ $\sqrt{\text{Hz}}$ in transverse displacement for frequencies $f > 150$ Hz in order that they not produce spurious noise in the gravitational wave readout channel. We show that seismic disturbances limit the use of local reference frames for angular alignment at a level approximately an order of magnitude worse than required. A wave-front sensing scheme that uses the input laser beam as the reference axis is presented that successfully discriminates among all angular degrees of freedom and permits the implementation of a closed-loop servo control to suppress the environmentally driven angular fluctuations sufficiently.

© 1998 Optical Society of America

OCIS codes: 120.3180, 120.2230, 220.1140, 000.2780.

1. Introduction

Currently several kilometer-scale gravitational wave interferometers are under construction around the world, all of which are expected to be operational near the end of the millennium. The Laser Interferometric Gravitational Wave Observatory¹ (LIGO) will consist of three interferometers operated simultaneously, two at a facility near Hanford, Washington, and one at a facility in Livingston Parish, Louisiana. The Variability of Solar Irradiance and Gravity Oscillations (VIRGO) detector is a single interferometer that is being built as a French-Italian project at Cascina, Italy²; a German-British group is constructing

an interferometer known as GEO 600 near Hannover, Germany;³ a Japanese collaboration is building a 300-m system near Tokyo.⁴ All these interferometers are variants of the Michelson interferometer as a detector of gravitational radiation⁵; the geometry is well matched to the quadrupolar strain in space that would be produced by a passing gravitational wave. The mirrors in the interferometer act as test masses of the space-time geometry; the proper distances between the test masses change proportionally to the amplitude of the gravitational wave. The test masses are made free by being suspended as pendula that typically have periods of 1 s. The differential change in proper distance between the interferometer's orthogonal arms produces a corresponding differential change in the phase of the laser light (i.e., a positive phase shift in one arm and a negative phase shift in the other). This differential phase shift is detected as an amplitude change in the light at the output of the interferometer.

A schematic of the optical configuration of the LIGO-VIRGO interferometers is shown in Fig. 1. The interferometers' optical design is an enhancement of the basic Michelson interferometer in several major respects. The arms contain Fabry-Perot cavities, each comprising a partially transmitting input mirror (which also serves as an inertially free test

When this research was performed, P. Fritschel, N. Mavalvala, D. Shoemaker, D. Sigg, and M. Zucker were with the Department of Physics and Center for Space Research, Massachusetts Institute of Technology, Cambridge, Massachusetts 02139, and G. González was with the Department of Physics, Pennsylvania State University, University Park, Pennsylvania 16802. N. Mavalvala is now with the LIGO Project, California Institute of Technology, MS 18-34, Pasadena, California 91125, and D. Sigg is now with the LIGO Project, P.O. Box 1970 S9-02, Richland, Washington 99352. (P. Fritschel's e-mail address is pf@tristan.mit.edu.)

Received 8 May 1998.

0003-6935/98/286734-14\$15.00/0

© 1998 Optical Society of America

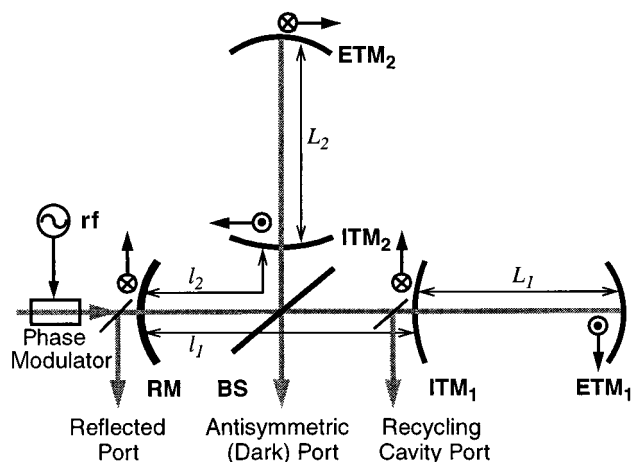


Fig. 1. Schematic optical layout of a power recycled interferometric gravitational wave detector. The input light is phase modulated with a rf waveform to generate error signals for the length and alignment degrees of freedom. The input test masses (ITM1 and ITM2) and the recycling mirror (RM) are partially transmitting mirrors, whereas the end test masses (ETM1 and ETM2) have maximum reflectivity; the beam splitter (BS) splits the light 50–50 between the two arms. The gravitational wave signal is derived from the light at the antisymmetric port; the recycling cavity port represents a small fraction of the light in the recycling cavity, which is typically provided by the antireflection-coated surface of the beam splitter or an ITM. Also indicated is the sign convention for the alignment angles. The symbol next to each optic shows the rotation axes (vectors) for horizontal and vertical tilts. A positive tilt angle corresponds to a right-handed rotation about the axis defined by the rotation vector.

mass) and a highly reflecting end mirror (and test mass), operated in resonance with the input laser light. The increased light-storage time in these cavities serves to increase the phase shift of the reflected light produced by arm-length changes.⁶ This configuration leads to the requirement that round-trip propagation phase in each cavity be $2n\pi$, where n is an integer. In addition, a partially transmitting recycling mirror is placed between the laser source and the beam splitter, which resonantly increases the optical power in the system, thereby enhancing the shot-noise-limited sensitivity.⁷ The optical path difference between the two arms is held equal to $2m\pi$ (m an integer), the Michelson dark-fringe condition in which the power at the antisymmetric port is a minimum; this procedure minimizes coupling to some technical noise sources and facilitates a recycling technique. The term “recycling cavity” is often applied to an optical system comprising a recycling mirror, two input test masses, and a beam splitter.

Thus the operating point of the interferometer is determined by the various light-propagation phases (or resonance conditions) in the system. There are four independent length degrees of freedom in the system. To maintain the best sensitivity of the instrument one must control these lengths to within small ranges—as small as 10^{-13} m, or 10^{-7} of the light’s wavelength—of this operating point. It is equally critical to maintain the mirror angles close to

the optimum point to maximize the power coupled into the optical system, maintain a good quality of interference at the antisymmetric interferometer port, and limit coupling to technical noise sources.

The technique for detecting these length degrees of freedom is briefly described here because an extension of it is used for detection of the alignment degrees of freedom; a more comprehensive description is given in Ref. 8. The input light is phase modulated at a ratio frequency f_m (typically 10–50 MHz) and with a relatively small amplitude, so only the carrier, at ν_0 , and the first-order modulation sidebands, at $\nu_0 \pm f_m$, have significant amplitudes among the series of modulation sidebands developed. The frequency f_m is chosen such that the sidebands are also resonant in the recycling cavity but are not resonant in the arm cavities. The detected photocurrents at various ports of the interferometer are then demodulated to give the zero-crossing error signals for the four lengths; the relative phases of the modulation and demodulation waveforms are additional degrees of freedom that can be adjusted for selection of an error signal. The in-phase signal derived from the reflected light is essentially equivalent to the traditional reflection locking technique for a single cavity⁹ and is sensitive predominantly to the average length of the arm cavities, $(L_1 + L_2)/2$, but also has some sensitivity to the recycling cavity length, $(l_1 + l_2)/2$. This signal is typically used in a high-gain loop to stabilize the input laser frequency. The in-phase signal derived from a sample of the recycling cavity light is similar to, but not quite collinear [in the $(L_1 + L_2, l_1 + l_2)$ space] with the reflected signal; it is also sensitive mostly to the average arm cavity length but has a different dependence on the recycling cavity length (it is sensitive to the difference in the finesse of the recycling cavity for the carrier and the sidebands). Furthermore, when the gain in the laser frequency stabilization loop is relatively high, this signal becomes sensitive only to the recycling cavity length.

The other two length degrees of freedom depend on the existence of a macroscopic asymmetry in the Michelson interferometer, $l_1 - l_2 \neq 0$, often called the Schnupp asymmetry,¹⁰ which breaks the symmetry between the reflection and the transmission sides of the beam splitter and allows signals proportional to length differences to be generated. Inasmuch as the dark-fringe condition holds for the carrier, the sidebands are not forcibly at a minimum at the antisymmetric port, and in fact the parameters are chosen such that most of the input sideband light is transmitted to this port. This antisymmetric port sideband light beats with any carrier light that is produced by a deviation from the dark fringe and thus gives a signal that is proportional to $[(L_1 - L_2) + (\pi/2F)(l_1 - l_2)]$, where F is the finesse of the arm cavities. The final length error signal uses the carrier as the reference field and derives from a change in the relative amplitudes of the sidebands that is produced by the degree of freedom $[(l_1 - l_2) + (\pi/2F)(L_1 - L_2)]$; this mode has the effect of increasing

the recycling cavity finesse for one of the sidebands and decreasing it for the other. This error signal appears in the quad phase of the photocurrent from both the reflected light and the recycling cavity light.

The six interferometer optics contribute an additional twelve angular alignment degrees of freedom to the system: the pitch and yaw angles of the four arm cavity mirrors, the beam splitter, and the recycling mirror. “Pitch” refers to the angle of motion about a horizontal axis; “yaw,” to the angle of motion about a vertical axis. The orientation of the beam splitter is not an independent variable, however, because the effect of its orientation on the angular alignment can be described in terms of the angles of input test mass ITM₂ and end test mass ETM₂. Similarly, the input beam’s direction is described by four additional degrees of freedom (displacement and tilt in each plane), but their effect on the angular alignment can be expressed in terms of the angles of the five interferometer optics. We thus have 10 independent angular alignment degrees of freedom. (The orientations of the beam splitter and the input beam are relevant later, when we consider transverse alignment, i.e., the transverse position of the beam on the finite-sized mirrors). The sign convention for these angles is defined in Fig. 1. The origins of the angles are defined at the point of optimal angular alignment, which in turn is defined as the point where the beam axis is collinear with the optic axes of the two arm cavities and the recycling cavity. A cavity optic axis is defined as the line through the centers of curvature of the cavity mirrors.

The pitch angle of an optic is designated θ ; the yaw angle, φ . Normalized optic angles are also used; these are the physical angles divided by the beam divergence angle in the arm cavities. The individual mirror angles present one basis for expressing the alignment; for pitch, $[\theta_{\text{ITM1}} \ \theta_{\text{ETM1}} \ \theta_{\text{ITM2}} \ \theta_{\text{ETM2}} \ \theta_{\text{RM}}]$, where RM is a recycling mirror. Another useful basis uses common and differential angles of the test masses and is obtained by a rotation of the above basis:

$$\begin{bmatrix} \Delta\theta_{\text{ETM}} \\ \Delta\theta_{\text{ITM}} \\ \frac{\theta_{\text{ETM}}}{\sqrt{2}} \\ \frac{\theta_{\text{ITM}}}{\sqrt{2}} \\ \text{RM} \end{bmatrix} \equiv \frac{1}{\sqrt{2}} \begin{bmatrix} 0 & -1 & 0 & 1 & 0 \\ -1 & 0 & 1 & 0 & 0 \\ 0 & 1 & 0 & 1 & 0 \\ 1 & 0 & 1 & 0 & 0 \\ 0 & 0 & 0 & 0 & \sqrt{2} \end{bmatrix} \begin{bmatrix} \theta_{\text{ITM1}} \\ \theta_{\text{ETM1}} \\ \theta_{\text{ITM2}} \\ \theta_{\text{ETM2}} \\ \theta_{\text{RM}} \end{bmatrix}. \quad (1)$$

Having defined the relevant degrees of freedom in the system, we proceed to discuss alignment effects in the LIGO. In Section 2 we analyze the effects of alignment on interferometer sensitivity and the resulting implications for alignment requirements. In Section 3 we present a scheme for detecting all the alignment angles by use of an extension of the phase modulation–demodulation technique used for length detection. In Section 4 we look at the alignment fluctuations that are due to environmental disturbances at the LIGO site and discuss the planned

servo control system of the mirror angles. The quantitative results given below apply to the initial LIGO interferometers, but the same treatment applies qualitatively to any power recycled, Fabry–Perot Michelson interferometer (such as the VIRGO). Relevant design parameters of the LIGO interferometers are given in Appendix A.

The formalism for calculating the effects of misalignment (as well as other types of optical beam distortion) in the interferometer has been developed in detail in the research reported in Ref. 11. The approach is to expand the electromagnetic field into Hermite–Gaussian modes, which are the eigenmodes of an ideal optical resonator with mirrors of infinite extent. Free-space propagators and misaligned optical components are represented by matrix operators that act on the state vectors in the basis, permitting calculation of the carrier and sideband fields at any plane in the interferometer, expressed in the Hermite–Gaussian basis. From the field values, the relevant detectable quantities are calculated. For small misalignments (when the normalized angles are much less than unity) the only modes that are significant in the expansion are the fundamental TEM₀₀ mode and the lowest-order transverse modes, TEM₁₀ and TEM₀₁. The pitch and yaw angles in the system are separable and are treated in the same way, so in much of the discussion to follow we treat explicitly misalignments in one plane only, and carry just the TEM₀₀ and TEM₁₀ modes.

2. Alignment Effects on Interferometer Sensitivity

A. Reduction of Sensitivity

We look first at how deviations from perfect alignment reduce the sensitivity of the instrument. In particular, it is the shot-noise-limited sensitivity that is degraded, because misalignments change the effective optical power in the interferometer. For the initial LIGO design, the sensitivity spectrum will be shot-noise limited for frequencies $f > 150$ Hz, so at issue is the degradation in this spectral region.

The shot-noise-limited sensitivity is made up of two parts: the signal sensitivity, which is the magnitude of the signal produced at the output by a strain, or differential arm-length change; and the shot noise that is due to the detected optical power. The shot-noise-limited sensitivity is the ratio of the shot noise to the signal sensitivity. The output signal is generated by the interference of the carrier and sideband fields at the output and so is proportional to the carrier and sideband field coupling into the interferometer. At the point of optimal alignment this coupling is a maximum and is first-order insensitive to the alignment. Thus if $S_{\text{sens}}(\boldsymbol{\theta})$ is the gravitational wave signal sensitivity as a function of misalignment angles $\boldsymbol{\theta}$ (a five-component vector when we consider only the horizontal or the vertical plane), it can be approximated at small angles by

$$S_{\text{sens}}(\boldsymbol{\theta}) = S_{\text{sens}}(0)(1 - \frac{1}{2} \boldsymbol{\theta} \mathbf{H} \boldsymbol{\theta}). \quad (2)$$

The Hessian matrix H is defined by

$$H_{ij} = \frac{d^2}{d\theta_i d\theta_j} S_{\text{sens}}(\boldsymbol{\theta}) \quad (3)$$

and is (up to a constant) the inverse of the covariance matrix $C = 2H^{-1}$. As the matrix H is symmetric, in general there are 15 coefficients to specify the sensitivity loss. However, noting that Eq. (2) describes a five-dimensional ellipsoid, we can reduce the problem to specifying five coefficients by using the principal axes of the (variance) ellipsoid. We do this by diagonalizing the covariance matrix C ; the eigenvectors u_i are the axes of the variance ellipsoid, and the corresponding eigenvalues σ_i^2 are the squares of the axes' lengths (i.e., the variances). Using the new basis u_i to express the mirror angles, we can then simply express the relative loss of sensitivity ε as

$$\varepsilon = 2 \sum_{i=1}^5 \left(\frac{\psi_i}{\sigma_i} \right)^2, \quad (4)$$

where ψ_i is the misalignment amplitude in the u_i direction and the factor of 2 accounts for misalignments in both pitch and yaw (assumed to be the same for a given u_i).

A two-mirror cavity will serve as a simple example of the above description. Consider a stable, two-mirror Fabry-Perot cavity, with a flat input mirror and a rear mirror with a radius of curvature R , spaced a distance L apart; the cavity is also characterized by its g parameter, $g = 1 - L/R$. The power buildup on a TEM₀₀ Gaussian beam incident upon the resonant cavity is given by the spatial overlap of the incident mode upon the mode sustained by the cavity. If the only mode mismatch is due to misalignment, so the cavity optic axis is misaligned with respect to the input beam axis, the overlap for small angles is

$$\begin{aligned} P(\theta_1, \theta_2)/P_{\text{max}} &\approx \exp[-R^2(g\theta_1 + \theta_2)^2/\omega_0^2] \\ &\times \exp[-LRg(\theta_1/\omega_0)^2] \\ &\approx 1 - \left(\frac{R}{\omega_0} \right)^2 (g\theta_1^2 + 2g\theta_1\theta_2 + \theta_2^2), \end{aligned} \quad (5)$$

where P_{max} is the power buildup with perfect alignment, θ_1 and θ_2 are the (pitch) angles of the front and back mirrors, respectively, and ω_0 is the cavity waist size—the $1/e$ radius of the field distribution.

For a given level of power coupling, $P(\theta_1, \theta_2)/P_{\text{max}} = \text{constant}$, relation (5) describes an ellipse, as shown in Fig. 2. The orientation of the ellipse and the ratio between the major and minor axes are determined completely by the g parameter. The most sensitive misalignment direction is $u_2 = \{\theta_1 \sin \alpha, \theta_2 \cos \alpha\}$, with α defined in Fig. 2. The ratio of the variances also depends only on g :

$$\sigma_1^2/\sigma_2^2 = \frac{1 + g + (5g^2 - 2g + 1)^{1/2}}{1 + g - (5g^2 - 2g + 1)^{1/2}}. \quad (6)$$

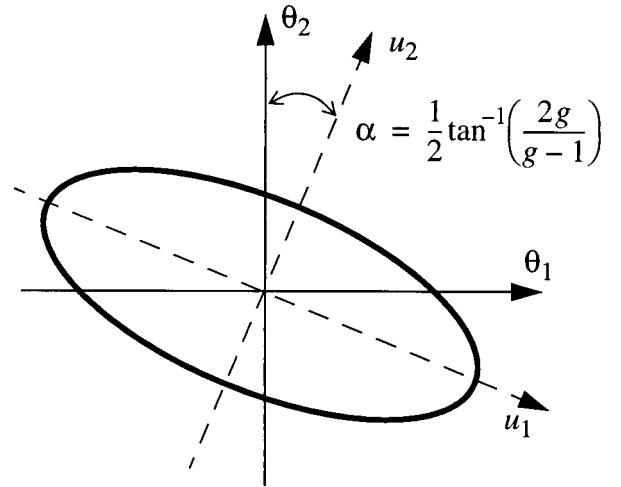


Fig. 2. Contour of reduction of power coupling with misalignment for a half-symmetric resonator. The ellipse's shape and orientation correspond to a cavity with $g = 1/3$ (at some arbitrary power reduction factor), for which $\alpha = \pi/8$ and $(\sigma_1/\sigma_2)^2 = 5.83$.

Returning to the problem of interferometer sensitivity loss, the first step is to compute the elements of matrix H as defined in Eq. (4). We do this numerically, using the modal model described in Section 1. The eigenvectors and the eigenvalues of the covariance matrix $C = 2H^{-1}$ then yield u_i and σ_i^2 , respectively. This procedure is applied to yield three useful pieces of information:

- (1) the signal strength of the gravitational wave output, S_{sens} ,
- (2) the noise level at the gravitational wave output, N , and
- (3) the signal-to-noise ratio of the gravitational wave output.

The interferometer signal-to-noise sensitivity is simply the ratio (S_{sens}/N) . The noise amplitude that is due to shot noise is proportional to the square root of the power detected:

$$N \sim (P_c + 3/2 P_{\text{sb}})^{1/2}, \quad (7)$$

where P_c and P_{sb} are the power levels of the carrier and sidebands, respectively, at the output port. (Most of the light power is from the sidebands; in this model the carrier interference at the beam splitter is perfectly destructive in the absence of misalignments.) The factor of $3/2$ in front of P_{sb} is due to the nonstationary characteristic of the noise.¹² The total power at the detector output may actually increase or decrease, depending on the type of misalignment; for small misalignments the change in output power, and thus the change in noise amplitude, is also quadratic in the misalignment. The signal and the noise depend differently on the angles, so these cases give three distinct covariance matrices.

The results of these calculations for the signal-to-noise ratio, when the LIGO parameters given in Ap-

Table 1. Eigenvalues and Eigenvectors of the Five-Dimensional Misalignment Variance Ellipsoid for the Shot-Noise-Limited Signal-to-Noise Ratio of the Interferometer^a

<i>i</i>	Eigenvalue σ_i^2	Eigenvector (Ellipsoid Axis)				
		ΔETM	ΔITM	$\overline{\text{ETM}}$	$\overline{\text{ITM}}$	RM
1	0.00061	0	0	0	-0.58	0.81
2	0.00050	0.91	0.42	0	0	0
3	0.12	-0.42	0.91	0	0	0
4	0.83	0	0	0.92	0.32	0.23
5	6.4	0	0	-0.39	0.75	0.54

^aThe eigenvalues are in units of (the square of) the beam divergence angle. Significant values are in boldface.

pendix A are used, are shown in Table 1. The eigenvalues σ_i^2 are given in normalized angle units, i.e., in units of the beam divergence angle in the arm cavities, $\theta_D = \lambda/\pi\omega_0 = 9.65 \times 10^{-6}$ rad, with $\omega_0 = 35.1$ mm.

The most sensitive misalignment mode for (S_{sens}/N) involves a differential misalignment of the ETM's against an ITM differential misalignment in the opposite direction. (The signs are the same in Table 1 because of the sign convention given in Fig. 1.) Nearly as sensitive is a common rotation of the ITM's against an opposite rotation of the recycling mirror. These two modes, u_2 and u_1 , are shown pictorially in Fig. 3. Separate calculations of the variance ellipsoids for the signal and the noise indicate the source of the degradation in each case. In mode u_2 , the sensitivity degradation is dominated by an increase in the shot noise; the TEM_{10} fields produced by the differential misalignment appear directly at the antisymmetric output and increase the noise-producing power.¹³

In mode u_1 , the signal is decreasing quickly, but the noise is also decreasing, although more slowly. The signal reduction is due mainly to reduction of the sideband field in the recycling cavity and thus at the antisymmetric port (which explains the decrease in noise, because it is due mainly to the sideband power). This relatively high sensitivity of the sideband field stems from the fact that, for the sidebands, the resonant frequencies of the higher-order Hermite–Gaussian modes in the recycling cavity are nearly degenerate with that of the TEM_{00} mode. This near degeneracy results from the very small ratio between the recycling cavity length (of the order of 10 m) and

the Rayleigh range of the beam (of the order of the arm's cavity length). This ratio determines the Gouy phase shift accrued by the nm th-order Hermite–Gaussian mode in traversing the recycling cavity:

$$\eta_{g,\text{rc}}(n, m) = (n + m + 1)\tan^{-1}(l_{\text{rc}}/z_0), \quad (8)$$

where l_{rc} is the recycling cavity length and $z_0 = \pi\omega_0^2/\lambda$ is the Rayleigh range. In the LIGO, $\eta_{g,\text{rc}}(0, 0) = 2.58$ mrad. This phase shift is to be compared with the phase width of the recycling cavity resonance, $\Delta\phi = \pi/F_{\text{rc}}$, where F_{rc} is the finesse of the recycling cavity. For the sidebands, $F_{\text{rc}} \approx 100$ and $\Delta\phi \approx 30$ mrad; thus all higher-order modes with $n + m \leq 10$ are essentially degenerate.

The power buildup of the fundamental mode of a near-degenerate cavity is much more sensitive to misalignment than for a nondegenerate cavity¹⁴; the sideband power thus degrades quickly. For the carrier there is an additional phase shift of π , which occurs on its reflection from the resonant arm's cavities. This reflection phase shift breaks the degeneracy for the carrier, because the higher-order modes do not experience it.

With the variances listed in Table 1 we can determine the alignment tolerances for a given degree of sensitivity loss from Eq. (4). Specifically, we impose a limit of $\epsilon = 0.5\%$, so misalignments produce a negligible loss of sensitivity. The most sensitive degrees of freedom, u_1 and u_2 , must then satisfy $\psi_1, \psi_2 \leq 10^{-3}$ rms (10^{-8} rad rms). Somewhat larger angles are permitted for the other degrees of freedom, up to $\sim 10^{-7}$ rad for u_4 and u_5 .

B. Parametric Noise Coupling

The second class of mechanisms by which alignment affects the interferometer sensitivity is parametric coupling of additional noise to which the perfectly aligned interferometer would be immune. Generally this immunity can occur through the coupling of some fluctuating system parameter with a misalignment in such a way as to produce a signal at the output that is proportional to the product of the misalignment angle and the fluctuating parameter. Such a bilinear coupling thus produces excess noise, which can contaminate the data stream. The importance of these noise mechanisms is gauged by comparison of them with the noise produced by the fundamental limiting noise sources in the interferometer, which determine the strain sensitivity goal for the LIGO. To ensure that the parametric noise mechanisms have a negligible effect on interferometer sensitivity, each noise mechanism is allowed an equivalent strain noise no greater than 1/10 (in amplitude) of this strain sensitivity goal.

The LIGO strain sensitivity is designed to be dominated by shot noise for frequencies $f \geq 150$ Hz at an equivalent strain noise of $h(f > 150 \text{ Hz}) \approx 2.5 \times 10^{-23} (f/150 \text{ Hz})/\sqrt{\text{Hz}}$.¹ This strain noise corresponds to fluctuations in the phase difference be-

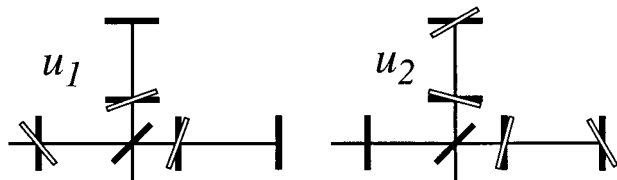


Fig. 3. Pictorial representation of the two most sensitive alignment degrees of freedom for the interferometer's shot-noise-limited signal-to-noise ratio. The filled bars represent the mirrors in the perfectly aligned interferometer, and the open bars indicate the (exaggerated) angles in the labeled mode.

tween the two arm fields at the beam splitter of $\delta\Phi_{bs}(f > 150 \text{ Hz}) = 8 \times 10^{-11} \text{ rad}/\sqrt{\text{Hz}}$ or to fluctuations in the length difference between the arms of $\delta L_-(f > 150 \text{ Hz}) = 10^{-19} (f/150 \text{ Hz}) \text{ m}/\sqrt{\text{Hz}}$. Below 150 Hz the sensitivity becomes poorer and is dominated by the thermal noise of the pendulum and internal modes; at 40 Hz the sensitivity in strain and displacement is $10\times$ worse than above, and it is $20\times$ worse in phase (seismic noise dominates at $f < 40 \text{ Hz}$). For the noise mechanisms considered here it is generally more convenient to make the comparison in terms of the differential phase shift.

Starting again with the example of a two-mirror cavity, the round-trip phase of the light Φ_{rt} is sensitive in second order to the mirror angles θ ; in matrix notation,

$$\Phi_{rt} = \Phi(\theta = 0) + \frac{1}{2} \theta H \theta, \quad (9)$$

where H is a 2×2 (Hessian) matrix. If angle θ contains a static part, $\Delta\theta$, and a fluctuating part, $\theta(t)$, the phase change at low frequencies (where H is frequency independent) is then

$$\delta\Phi_{rt}(t) = \frac{1}{2} \Delta\theta H \Delta\theta + \Delta\theta H \theta(t) + \frac{1}{2} \theta(t) H \theta(t). \quad (10)$$

The first term above represents static change in the phase, and the last term is second order in the fluctuating angle (typically much smaller than the static angle). The middle term is the one of interest, as it gives a linear sensitivity to the fluctuating angle.

For the interferometer, the matrix H becomes a 5×5 matrix and can be calculated numerically from the modal model. In the modal picture a signal is produced when the static TEM_{10} mode generated by the misalignment of one mirror is transformed back into a fluctuating TEM_{00} mode by a fluctuating misalignment of another (or the same) mirror. This fluctuating TEM_{00} mode may then appear at the antisymmetric port and produce a signal.

With the matrix H in hand, we calculate its eigenvalues and eigenvectors. The magnitude of the amplitude spectral density of the phase difference at the beam splitter for the most sensitive degrees of freedom is

$$\delta\Phi_{bs}(f) = 8 \times 10^{-11} \frac{\text{rad}}{\sqrt{\text{Hz}}} \sum_{i=1}^2 (-1)^i \left(\frac{\alpha_{i,\text{rms}}}{10^{-8} \text{ rad}} \right) \times \left[\frac{\alpha_i(f)}{7 \times 10^{-16} \text{ rad}/\sqrt{\text{Hz}}} \right], \quad (11)$$

where $\alpha_{i,\text{rms}}$ is the static or root-mean-square magnitude and $\alpha_i(t)$ is the amplitude spectral density of the angle $\alpha_i = 0.67\theta_{\text{ITMi}} + 0.74\theta_{\text{ETMi}}$. This expression implies an upper limit of $\alpha_i(f > 100) \leq 7 \times 10^{-17} \text{ rad}/\sqrt{\text{Hz}}$ for the angular fluctuations allowed in the suspended test masses. Estimates for the angular motion of the test masses at 100 Hz are safely below this: Brownian motion of the pitch and yaw modes is estimated at $3 \times 10^{-18} \text{ rad}/\sqrt{\text{Hz}}$,¹⁵ and seismically

driven fluctuations are expected to be even smaller, at $10^{-19} \text{ rad}/\sqrt{\text{Hz}}$. The next most sensitive pair of eigenvectors also involves the input and end test masses but with opposite relative signs; their eigenvalues are four times smaller than above. Here we have assumed that the rotation axes of the mirror angles lie in the reflecting surfaces of the mirrors and have their origins at the center of the beam. In reality the center of rotation of a mirror lies $\sim 5 \text{ cm}$ behind the surface, and the laser beam might hit the mirror off center. The former effect makes a negligible addition to Eq. (10), and the latter effect is discussed further below.

We see that the parametric coupling between static mirror angle and fluctuating mirror angle produces a signal that is negligible compared with the shot noise [Eq. (11)], given the required level of alignment and the expected mirror angle fluctuations. A related effect involving fluctuations of the input beam direction, however, is not insignificant. Note that the angles in Eqs. (9)–(11) are defined with respect to the perfectly aligned condition, which is determined by the direction of the input laser beam. This is a complete description because a change in the input beam direction can be equivalently described by a combination of mirror angles. Thus, if we used H to compute $\delta\Phi_{bs}(t)$ of Eq. (10) when the angle vector $\theta(t)$ corresponds to a tilt or displacement of the input beam, we find the sensitivity of the interferometer to fluctuations of the input beam direction (also called beam jitter) in the presence of static mirror misalignments $\Delta\theta$. As this is an important effect, we treat it more explicitly in the following paragraphs.

The input beam direction is described by the tilts (α_{ib} and β_{ib}) and displacements (x_{ib} and y_{ib}) of the beam in the (x, y) directions at the recycling mirror (with the perfectly aligned condition determining the origin). The tilts are expressed in units of the beam divergence angle θ_D , and the displacements are in units of the beam waist size in the arm cavities, ω_0 . In one dimension, the input beam is then written in terms of the fundamental TEM_{00} and first-order TEM_{10} modes as follows:

$$E_0(x, z, t) = \left(\left(1 - \frac{x_{ib}^2}{2} - \frac{\alpha_{ib}^2}{2} \right) U_0(x, z) + \{x_{ib}(t)[1 + i(z/z_0)] - i\alpha_{ib}(t)\} U_1(x, z) \right) e^{i\omega t}, \quad (12)$$

where U_0 and U_1 are the fundamental and first-order Hermite–Gaussian modes in one dimension, with propagation direction along z , and z_0 is the beam's Rayleigh length.

The modal model calculation yields the following result for the signal produced by beam jitter–

misalignment coupling, in terms of the equivalent differential phase $\delta\Phi_{bs}$:

$$\delta\Phi_{bs}(t) = 2.6 \times 10^{-11} \left\{ \left(\frac{0.91\Delta\theta_{ETM} + 0.41\Delta\theta_{ITM}}{10^{-8} \text{ rad}} \right) \left[\frac{\alpha_{ib}(t)}{10^{-8}} \right] + 0.19 \left(\frac{0.90\Delta\theta_{ETM} + 0.43\Delta\theta_{ITM}}{10^{-8} \text{ rad}} \right) \left[\frac{x_{ib}(t)}{10^{-8}} \right] \right\} \text{ rad.} \quad (13)$$

The input beam tilt and displacement couple to nearly the same misalignment mode, though the tilt sensitivity is approximately five times larger than the displacement sensitivity. The coupling is almost exactly along one of the interferometer sensitivity ellipsoid eigenvectors—the mode u_2 defined in Table 1. The terms proportional to the other alignment degrees of freedom (the recycling mirror and common mode angles) are negligible compared with the test mass differential angles.

If the beam jitter signal is to be much ($10\times$) smaller than the shot-noise-limited sensitivity given above in the presence of a $\psi_{2\theta_D} = 10^{-8}$ rad misalignment, we require that the input beam fluctuations be limited at

$$\begin{aligned} x_{ib}, y_{ib} &< 8.1 \times 10^{-9} / \sqrt{\text{Hz}}, \\ \alpha_{ib}, \beta_{ib} &< 1.5 \times 10^{-9} / \sqrt{\text{Hz}} \end{aligned} \quad (14)$$

for frequencies $f > 150$ Hz. This assumes that the beam tilt and displacement terms in Eq. (13) contribute equally, corresponding to fluctuations of less than 1.5×10^{-14} rad/ $\sqrt{\text{Hz}}$ in tilt and 2.8×10^{-10} m/ $\sqrt{\text{Hz}}$ in displacement in each direction. We attain this level of stability by passing the laser beam through a mode cleaner—a suspended Fabry–Perot cavity operated in vacuum, which efficiently transmits the resonant TEM_{00} mode and suppresses nonresonant higher-order modes.¹⁴

The above discussion does not address all dynamic effects associated with the fluctuating parameter in question because the coupling terms—described by the matrix H —can have a frequency dependence themselves. In the case of input beam jitter, for example, we wish to consider the effect of a direction-modulated input beam, given generally by

$$x_{ib}(t) = x_0 \cos(\omega_a t), \quad \alpha_{ib}(t) = \alpha_0 \cos(\omega_a t). \quad (15)$$

We treat this effect in the frequency domain by expressing the U_1 component as two audio sidebands separated by angular frequencies $\pm\omega_a$ with respect to the U_0 component, each of amplitude $\{x_0[1 + i(z/z_0)] - i\alpha_0\}/2$. There are then fields at three discrete frequencies, $\{\omega_0, \omega_0 + \omega_a, \omega_0 - \omega_a\}$. The phase modulation adds a pair of rf sidebands to each of these fields, resulting in nine frequencies that are propagated through the interferometer. By varying the modulation frequency ω_a we calculate the frequency response of the antisymmetric output to beam jitter coupled to misalignment. Such a calculation shows that the coupling produces a differential phase noise that is nearly independent of frequency from $\omega_a = 0$

to several kilohertz; the coupling values given above are thus valid in the relevant gravitational-wave band. A similar conclusion holds for the second-order signal that is due to fluctuating mirror angles.

The reason that there is a negligible frequency dependence in these effects is that there is a separation between the TEM_{00} and the TEM_{10} eigenfrequencies in the arm cavities—the TEM_{10} resonant modes of the arm cavities are shifted by 11.4 kHz from the TEM_{00} modes. Thus the TEM_{10} modes generated by the misalignments are generally not resonant in the arm or recycling cavities; only for mirror angle or input beam modulation frequencies at or near $\omega_a = 2\pi \times 11.4$ kHz is there a peak in the response, but this is above the interesting gravitational wave frequency band. The rf sideband TEM_{10} modes are resonant in the recycling cavity because of its near degeneracy, as discussed above, but this is a broad resonance (~ 100 -kHz width) and thus does not influence the frequency response in the kilohertz region.

The last type of parametric noise that we consider is the coupling of angular fluctuations with a displacement of the optic axis of a cavity from the centers of rotation of the mirrors. Even with perfect angular alignment, such a transverse misalignment permits a first-order sensitivity to angular fluctuations of the mirrors, an effect that has been treated in detail in Ref. 16. To first order, the perturbation to the optic axis length that is due to a given mirror is simply the displacement of the beam centroid from the mirror's center of rotation, d_{CoR} , multiplied by the angular fluctuation of the mirror $\alpha(t)$, about an axis perpendicular to the displacement vector: $\delta L(t) = d_{\text{CoR}}\alpha(t)$. This effect determines how well the optic axes must be aligned with the mirrors' centers of rotation. In the presence of angle fluctuations (dominated by thermal noise) of $\alpha(100 \text{ Hz}) = 3 \times 10^{-18}$ rad/ $\sqrt{\text{Hz}}$ on all four test masses, we must maintain the beam position within a radius of 1 mm of the test mass centers of rotation to keep this noise signal an order of magnitude smaller than the shot-noise level in the LIGO.

3. Alignment Detection

An extension of the phase modulation–demodulation length-sensing technique for detecting angular misalignments was developed recently in the research reported in Refs. 11 and 17. In this scheme an output beam is detected with a multielement photodetector, which can spatially resolve any amplitude modulation present at the phase-modulation frequency. Misalignments in the optical system produce such a spatial amplitude modulation and are detected in the demodulated signals from these photodetectors (the term “wave-front sensor” is used to denote such a photodetector–demodulator system). The misalignment signal is essentially produced by the interference of the fundamental TEM_{00} mode of the carrier (sidebands) and the misalignment-generated TEM_{10} and TEM_{01} modes of the sidebands

Table 2. Alignment Sensing Parameters Defined in Eq. (16) for Each Sensing Port^a

Sensing Port	Angular Degree of Freedom				
	ΔETM	ΔITM	$\overline{\text{ETM}}$	$\overline{\text{ITM}}$	RM
Antisymmetric	-25 Q 90°	-11 Q 90°	-9.9×10^{-6} Q 156°	-4.5×10^{-6} Q 156°	-1.2×10^{-3} Q 90°
Reflected	2.3×10^{-2} Q 144°	-1.4 Q 144°	-0.73 I 97°	6.2 I 146°	-9.6 I 146°
Recycling cavity	1.8×10^{-3} Q 144°	-0.11 Q 144°	1.4×10^{-2} I 61°	0.52 I 143°	-0.72 I 144°
Reflected (NR sidebands)	-1.5×10^{-4} I 148°	-1.7×10^{-3} Q 0°	-2.1 I 90°	-0.97 I 90°	1.9 I 0°

^aFor each angular degree of freedom, the top number listed is A_i (in watts, with significant values in boldface); below left is the RF phase ϕ_{Di} , in phase (I) or in quadrature (Q) with the modulation phase at the input, and below right is the Gouy phase angle η_i . The last row lists the signals produced with phase-modulation sidebands that are not resonant (NR sideband) in the interferometer.

(carrier). Because the interference signal depends on the cosine of the Gouy phase angle between the TEM_{00} and the TEM_{10} modes, the other spatial degree of freedom—the longitudinal position of the detector along the optic axis—is also relevant. This means that one can distinguish angular misalignments of longitudinally separated optical elements by placing multielement detectors at different positions along the optical path. To detect both pitch and yaw misalignments, a quadrant photodetector would typically be used.

For a single, nondegenerate cavity, two wave-front sensors can be placed such that one is sensitive only to misalignments of the front mirror and the other senses only the back mirror. For a complete interferometer, however, such a separation does not occur; a wave-front sensor at a particular location is generally sensitive to misalignments of all the mirrors in the system. The problem is to determine a set of wave-front sensors that yields a nonsingular matrix of alignment signals, so that angular misalignments of all the individual elements can be determined.

Sensing the three interferometer output ports shown in Fig. 1 (which give the four length signals) determines the angular alignment information obtainable with multielement detectors. At any port, we write the radio frequency amplitude-modulated alignment signal in the form

$$\begin{aligned} \text{WFS}(\eta, \Theta, \Gamma) &= P_{\text{in}} f(\Gamma) f_{\text{split}} k_{\text{PD}} \\ &\times \sum_{i=1}^5 A_i \Theta_i \cos(\eta - \eta_i) \cos(\omega_m t - \phi_{Di}), \end{aligned} \quad (16)$$

where, for the i th angular degree of freedom, Θ_i is the normalized misalignment angle, the coefficient A_i is the rf-modulated component of the optical power that is due to the interference of TEM_{00} and TEM_{10} modes, ϕ_{Di} is the phase of the signal at the modulation frequency ω_m (with respect to the phase of the impressed phase modulation), and η_i is the Gouy phase between the TEM_{00} and TEM_{10} modes at the

output port. The variable parameter η is any additional Gouy phase shift that is due to the detector's longitudinal position. The coefficients A_i are calculated when the intensity is integrated over a half-plane detector, which is one that subtracts and integrates over two mirror-symmetric half-infinite planes located left and right of the y axis. The modulation index is incorporated into the factor $f(\Gamma) \equiv 2J_0(\Gamma)J_1(\Gamma)$, which for low modulation index reduces to $f(\Gamma) \approx \Gamma$ (A_i is independent of the modulation index). The input power is P_{in} , the fraction of a particular port's light that is directed to the wave-front sensor is f_{split} , and k_{PD} is a less-than-unity factor that accounts for the difference between the specific photodiode geometry and the idealized half-plane detector. WFS is the wave-front sensor.

The alignment matrix and the associated Gouy and rf phases calculated for the LIGO configuration are given in Tables 2 and 3, where the units of A_i are watts, normalized to 1 W of total input power. A_i for the recycling cavity port includes a factor of 3×10^{-4} , which represents the fraction of the recycling cavity internal power (~ 300 W) that is directed out of the recycling cavity by, e.g., the antireflection-coated first surface of one of the input test masses. The first three rows of Table 2 list the alignment signals produced by the interference of the carrier light with the main RF modulation frequency f_m (the frequency used to detect the length degrees of freedom, including the gravitational wave signal). The last row lists the signals produced by the carrier interfering with a second modulation frequency, f_{NR} ; this frequency is chosen such that its modulation sidebands are not resonant in any part of the interferometer; they are directly reflected from the recycling mirror. As the table shows, these signals are essential for distinguishing a misalignment of the recycling mirror from a common mode misalignment of the input test masses, because there is no Gouy phase separation between these degrees of freedom in the carrier-resonant sideband interference terms.

As expected, differential misalignments show up at

Table 3. The Five Wave-Front Sensor Signals for a Specific Choice of Sensor Positions, Gouy Phases, and RF Phases^a

Wave-Front Sensor Number	Port	η (°)	ϕ_D^b	Degree of Freedom Detected	Magnitude (W) A_{WFS}
1	Antisymmetric	90	Q	$u_2 = 0.91\Delta\theta_{\text{ETM}} + 0.42\Delta\theta_{\text{ITM}}$	28
2 a	Recycling cavity	145	I	$u_1 = 0.81\theta_{\text{RM}} - 0.42\theta_{\text{ITM}}$	0.89
b			Q	$\Delta\theta_{\text{ITM}}$	0.11
3	Reflected	0	I	θ_{RM}	1.9
4	Reflected	90	I	$0.91\theta_{\text{ETM}} + 0.42\theta_{\text{ITM}}$	2.3

^aThis set of five signals gives a nondegenerate sensing matrix for all the relevant angular degrees of freedom. The magnitude of these signals, A_{WFS} , is given in watts and is normalized in the same way as the A_i in Table 2.

^bI, in phase; Q, in quadrature.

the antisymmetric port; however, only one degree of freedom emerges—a combination of ETM and ITM differential angles. This result is due to the dark-fringe condition, which ensures that there is no carrier TEM_{00} component at this port. Thus there is no term proportional to the interference between the carrier TEM_{00} and the sideband TEM_{10} modes, which is normally the term that separates the front from the back mirror in an isolated cavity. The other differential mode shows up on the other side of the beam splitter, at the reflected or recycling cavity port. Here there is a significant level of sideband TEM_{10} mode, as a result of the Michelson asymmetry, which interferes with the carrier TEM_{00} mode.

The reflected and recycling cavity signals that are due to resonant sideband and carrier interference are dominated by the high angular sensitivity of the sidebands in the near-degenerate recycling cavity. The TEM_{10} modes of the resonant sidebands, produced by a misalignment of either the recycling mirror or the common mode input test masses, are built up in the recycling cavity; carrier TEM_{10} modes, however, experience no such resonant build up. Consequently, the carrier-resonant sideband alignment signals for common ITM and RM motions are much larger than that for common ETM motion, which produces only a carrier TEM_{10} mode. Furthermore, these large alignment signals have the same intrinsic Gouy phase, because there is no Gouy phase accrual in the recycling cavity for the sideband TEM_{10} modes.

The situation for the nonresonant sidebands signals is nearly the converse. Inasmuch as these sidebands do not enter the interferometer, no sideband TEM_{10} mode is produced by either common ITM or ETM motions; the signals produced by these angles are due entirely to interference between a carrier TEM_{10} mode and the nonresonant sideband TEM_{00} mode. The common ITM and ETM signals thus have the same Gouy phase angle, and it is different from that for the recycling mirror signal (because, as noted above, the carrier TEM_{00} and sideband TEM_{10} interference term is the one that separates the front from the back mirror in an isolated cavity). The signal amplitudes for common ITM and ETM angles are also comparable, given the absence of the nonresonant sidebands in the recycling cavity; the common ITM—common ETM signal ratio is given by the cavity parameter $g_2 = 1 - L/R_{\text{ETM}} = 0.46$, where L

is the arm cavity length (4 km) and R_{ETM} is the radius of curvature of the end test mass (7400 m).

A convenient feature of the alignment signal matrix is that two of the detectors sense the two directions that are most critical to the interferometer sensitivity. These detectors are the antisymmetric port detector, which is sensitive to the u_2 direction, and the I -phase recycling cavity or reflected port detector, which is sensitive along u_1 . Note that the former is also the direction to which beam jitter couples.

The fundamental limit to the angle sensitivity of these alignment error signals is due to the shot noise in the detection photocurrent. We define the angle sensitivity $|S_{\text{WFS}}|$ for a given wave-front sensor, in units of watts per radian, as

$$|S_{\text{WFS}}| = P_{\text{in}} f(\Gamma) f_{\text{split}} k_{\text{PD}} A_{\text{WFS}} / \theta_D, \quad (17)$$

where the A_{WFS} coefficients are defined in Table 3.

The shot noise is determined by the total optical power on a given sensor:

$$N_j \approx 2(e\eta P_j / h\nu_0)^{1/2}, \quad (18)$$

where e is the electron charge, h is Planck's constant, P_j is the total power detected by sensor j , η is the quantum efficiency of the photodiode, and the approximation has been made that the power is constant in time. We then define the angle-equivalent shot-noise sensitivity as

$$\tilde{\alpha}_{\text{WFS}} = (N_j h\nu_0) / (\eta |S_{\text{WFS}}|). \quad (19)$$

To compute the sensitivities of the wave-front sensors we use an input power $P_{\text{in}} = 6$ W, a diode quantum efficiency $\eta = 60\%$, and a geometry factor of $k_{\text{PD}} = 0.7$ (corresponding to a quadrant detector). The splitting ratios and modulation factors are different for the various sensors and are given in Table 4 along with the sensitivities. We conclude that the wave-front sensors are sufficiently sensitive to detect the relevant misalignment angle of 10^{-8} rad (the fluctuations of which are confined to an ~ 10 -Hz bandwidth, as discussed below), and in fact that they have several orders of magnitude of margin. When electronic noise in the photodiode amplifier is taken into account, a comfortable margin is still maintained.

The frequency response of the alignment signals can be calculated by the audio sideband technique

Table 4. Wave-Front Sensor Angle and Angle-Equivalent Shot Noise Sensitivities^a

Wave-Front Sensor Number	f_{split}	$f(\Gamma)$	$ S_{\text{WFS}} $ (W/rad)	$\tilde{\alpha}_{\text{WFS}}$ (rad/ $\sqrt{\text{Hz}}$)
1	0.01	0.5	6.0×10^4	1.1×10^{-15}
2a	1	0.5	1.9×10^5	1.3×10^{-15}
2b	1	0.5	2.4×10^4	1.0×10^{-14}
3	0.01	0.05	425	9.6×10^{-14}
4	0.01	0.05	508	8.0×10^{-14}

^aThe splitting factors for the sensors at the antisymmetric and the reflected ports (wave-front sensors 1, 3, and 4) are small, so most of the light can be directed to the length sensors; for the recycling cavity port sensor (wave-front sensors 2a and 2b), the splitting factor is unity because there are other antireflection surface beams available for the length sensor. Sensors 3 and 4 use the nonresonant sideband for detection, for which the modulation index is chosen to be 1/10 that of the main modulation frequency.

described above. A mirror that is modulated in angle at an angular frequency ω_a with an amplitude α will generate a time-varying TEM_{10} mode from an incident TEM_{00} mode as follows:

$$M(t) \otimes U_0 = [1 - 4\alpha^2 \cos^2 \omega_a t] U_0 + 2i\alpha \cos \omega_a t U_1, \quad (20)$$

where $M(t)$ is the mirror operator.¹¹ Just as there is no frequency dependence of the input beam jitter coupling into the gravitational wave signal at low frequencies, the alignment signals are effectively independent of frequency up to several kilohertz. Only when the audio frequency is equal to the transverse mode spacing in the arm cavities (11.4 kHz) will the TEM_{10} carrier mode resonate and produce a peak in the frequency response. Specifically, at this point only one of the two audio sidebands resonates; the other resonates when the audio frequency is equal to the difference between the arm's free spectral range and the mode spacing (37.5 kHz – 11.4 kHz = 26.1 kHz). These features are high enough in frequency that they are irrelevant to the alignment control system, which is described in Section 4.

So far we have neglected the angular degrees of freedom of the beam splitter and the input beam direction, because misalignments in these degrees of freedom can be compensated for by a realignment of the other interferometer mirrors, leaving the system with the same angular alignment. Such a realignment, however, changes the transverse alignment as the beam center moves away from the centers of rotation of the optics. Because these offsets at the four test masses must be below 1 mm, as discussed at the end of Section 2, additional detectors are needed to monitor the transverse beam positions on these optics. Because the walk-off effect is most severe on the end test masses, two position-sensitive (quadrant) photodetectors measuring the transmitted beams of the arm cavities are used to detect the lateral beam positions at these points. A change of the beam-splitter orientation will shift the beam position on ETM_2 , whereas a change of the input beam direc-

tion will shift the beam position on both ETM 's. The angles of the beam splitter and the input beam must be within $\sim 10^{-7}$ rad of the optimal point to maintain adequate beam centering.

4. Alignment Fluctuations and Control

In Section 2 it was shown that the mirror angles must be stabilized within $\sim 10^{-8}$ rad of optimal alignment to maintain the interferometer sensitivity, and in Section 3 a wave-front sensing system capable of determining the point of optimal alignment with sufficient accuracy was presented. To establish requirements for the control systems charged with correcting and maintaining these angles we examine the various forces that act on the mirrors that cause angular fluctuations. Finally, a feedback control design that counteracts these external forces to maintain the required alignment continuously and automatically is described.

A. Environmentally Induced Fluctuations

In the LIGO the cylindrical mirrors are suspended by a continuous single wire sling, both ends of which are clamped to a rigid support. The free length of the wire is chosen to afford a pendulum eigenfrequency of 0.74 Hz; the separation of the wire ends at the clamp and the height of the wire's departure from the cylindrical mirror surface are chosen to give pitch and yaw eigenfrequencies of approximately 0.5 Hz. Mirror displacement, pitch, and yaw control forces are all applied through electromagnetic actuators, each comprising a permanent magnet attached to the mirror surface and a copper coil mounted to the pendulum support. Currents in the four coils acting on each mirror are provided in common to produce the desired mirror displacement and differentially to produce corrective torques. The suspension's pendulum, pitch, and yaw modes are designed to have minimal mechanical dissipation to reduce the influence of Brownian thermal noise. Each of the suspension supports is in turn mounted upon a passive seismic isolation system consisting of four serial stages of damped mass-spring mechanical oscillators.¹⁸

Environmental forces that produce angular fluctuations arise predominantly from motions of the seismic isolation system's foundation, which are applied to the mirror by means of the dynamic responses of the isolation and suspension systems. Thermal expansion and inelastic relaxation (creep) of mechanical support components may also alter the alignment over time. We have constructed a model of the system that incorporates the dynamics of the isolation and suspension systems and includes measurements or models of these environmental inputs. The most significant input to the model is the ground motion that drives the isolation stacks. For this input we introduce recorded seismometer measurements of the ground motion taken at the two LIGO sites, Hanford, Washington, and Livingston Parish, Louisiana.¹⁹ We also include an estimate of how the facility foundation responds to ambient thermal and barometric and acoustic pressure changes. These

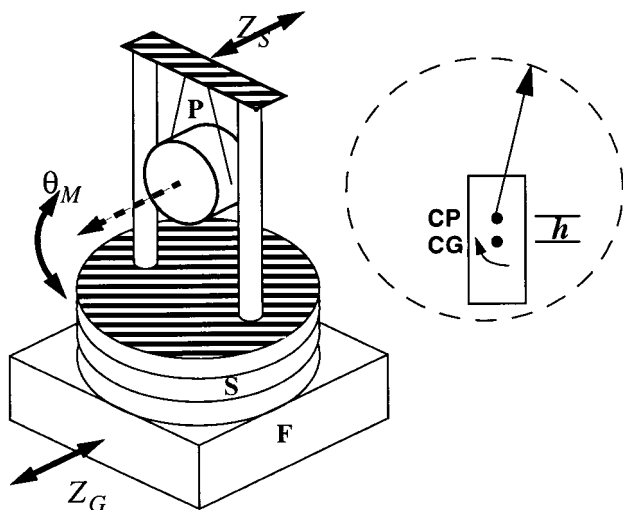


Fig. 4. Schematic of a LIGO test mass and its support, isolation, and suspension systems. The dominant angular motion of the mirror is expected to be in pitch, θ_M , and is induced primarily by translation Z_G of the facility foundation F, causing translation of the seismic isolation stack S and thus of the pendulum suspension point. The wire sling suspension P converts this translation into a torque (inset). The pivot point P where the wire is joined to the test mass lies a small distance h above its center of gravity CG. (h is chosen to make the mirror gravitationally stable with an appropriate pitch eigenfrequency.) Acceleration of the suspension support (S) thus induces a torque about the mirror's pitch axis.

excitation sources are provided as the inputs to linear transfer function matrix elements computed for the planned LIGO seismic isolation stacks, calculated by finite-element analysis.²⁰ The resultant motion of the optics support plate (in four degrees of freedom), including the motion of the suspension point, is then provided as input to a transfer matrix for the pendulum suspension system, which then predicts the induced mirror angles.

Ground vibration amplitude is dominated by motion at the microseismic frequency of 0.15 Hz; the amplitude varies during the year and is different at the two LIGO sites but is typically $\sim 1 \mu\text{m}_{\text{rms}}$. At frequencies below 10 Hz, displacements of the mirror are dominated by the corresponding ground motion, multiplied by the appropriate stack transfer function (for example, the motion along the optic axis is due mainly to ground motion along this direction, multiplied by the horizontal–horizontal stack transfer function). Rotations, on the other hand, arise mostly from off-diagonal couplings in the stack and suspension, which are excited by ground translation. For example, we find that the dominant environmentally induced angular fluctuation of a LIGO test mass arises from seismic translation, as shown in Fig. 4: horizontal motion of the facility foundation and isolation stack accelerates the suspension support point, pulling the suspension wires away from vertical, which then couples a small torque that is due to the gravitational restoring force. The original tilt and yaw motions of the ground are estimated to make

significantly smaller contributions to the angle fluctuations than these cross-coupled components.

B. Alignment Control

We conclude by presenting a scheme for applying the wave-front sensing method described in Section 3 to control the mirror angles in the face of the environmental disturbances described above. A prototype control system using this sensing method to control all 10 angular degrees of freedom of a tabletop model interferometer was recently demonstrated.²¹

For the LIGO and other full-scale interferometers, the suspension and seismic isolation systems introduce significant added complications, both in the nature of expected disturbances (as described above) and in the available means of actuation. In addition, it is critical that imperfections in the alignment control system not introduce significant noise into the mirrors, especially at frequencies that correspond to the active gravitational wave search band (40 Hz–10 kHz). For example, excess electronic noise might induce torque on a mirror that exceeds the baseline given by Brownian thermal fluctuations, thus introducing apparent length fluctuation by means of de-centering. Fortunately, as we have seen, the predominant environmentally induced alignment fluctuations occur at frequencies below 10 Hz, so it is possible to confine the control system's action (and thus any deleterious side effects) to a restricted bandwidth that is distinct from the search band.

By extending the angular excitation model described above to include control feedback forces, we modeled such a control system for the LIGO and showed that the required alignment accuracy can indeed be achieved and maintained in practice. The wave-front sensor inputs (WFS 1–4; Table 4) described in Section 3 must be linearly combined to yield the appropriate corrective torque for each of the interferometer mirrors and the incident beam direction. This process is accomplished by a matrix transformation. The coefficients of this transformation are readily calculated, but it is expected that adjustments may be required to account for variations in the system (which arise, for example, from varying optical losses or differential variation in the force coefficients of individual mirror actuators). We determine these updates by applying calibrated probe torques to individual mirrors or combinations and then inverting the response function measured by the wave-front sensors.

The dynamic control compensation is designed specifically to counteract the expected disturbances described above while affording robust closed-loop stability and preventing infiltration of controller or residual sensing noise in the active search bandwidth. To illustrate the features of this compensation we consider an equivalent single-input–single-output control loop (Fig. 5).

Two tuned resonant sections are included to boost the gain locally at most troublesome disturbance frequencies. One such section, tuned to 0.15 Hz and with a fractional bandwidth $Q^{-1} \approx 0.3$, counteracts

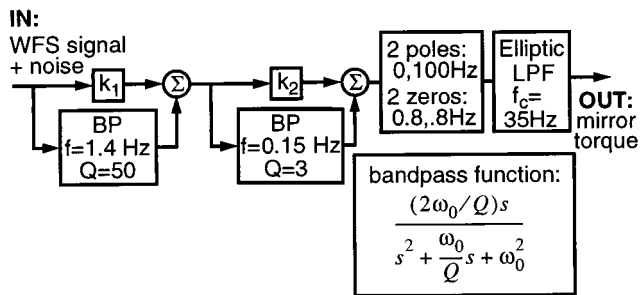


Fig. 5. Block diagram of electronic compensation for an equivalent single-input-single-output loop design to control one composite angular degree of freedom (for example, u_1). The control compensation is tailored to counteract the microseismic motion (which peaks at 0.15 Hz) and the expected resonant amplification of the seismic isolation stacks (at their eigenfrequency of 1.4 Hz) by inclusion of two tuned resonant gain sections. Sharp low-pass filtering above the 5.2-Hz unity gain frequency is provided to prevent infiltration of residual sensing (e.g., photocurrent shot) and electronic noise in the LIGO measurement band, above 40 Hz. BP's, bandpass filters; LPF, low-pass filter; WFS, wave-front sensor.

the microseismic motion, which has a strong peak at this frequency (corresponding to the average frequency of ocean waves striking the continental shores). A second resonant section, at 1.4 Hz, is tuned to counteract the lowest expected resonant mode of the LIGO seismic isolation system, which is expected to have a fractional width $Q^{-1} \approx 0.02$. Specific targeting of other modes of the seismic isolation system did not prove necessary in this design example but is relatively straightforward to implement, if required, by extension of the approach shown in Fig. 5.

With this type of control characteristic in place, the residual errors in mirror alignment are as shown in Fig. 6 (bottom). Integration of this residual error spectral density yields a root-mean-square alignment error of 8×10^{-9} rad, consistent with the requirement.

5. Summary and Conclusions

We have identified the important physical effects of misalignment that can cause the gravitational wave sensitivity in the LIGO to deteriorate: Static angular misalignment can decrease the power buildup in the arm cavities or can increase the shot noise at the antisymmetric port, input beam jitter can couple through a static misalignment directly into the gravitational wave readout, and angular fluctuations can be transformed into displacement noise when the laser beam hits one of the interferometer mirrors off center. We require that the noise level introduced by alignment degrees of freedom lie at least a factor of 10 below the LIGO target noise floor. This corresponds to a degradation of the signal-to-noise ratio of no more than 0.5%, which has a negligible effect on the observatory's astrophysical sensitivity. We have shown that achieving this small degradation in signal-to-noise ratio requires that the angular align-

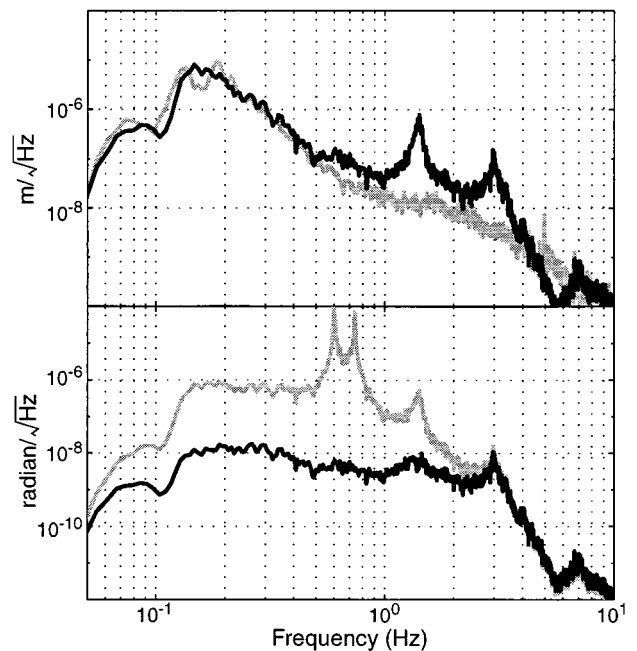


Fig. 6. Top, spectral density of ambient horizontal seismic vibration measured at the Livingston, Louisiana, LIGO site (gray curve; this is the Z_G input in Fig. 4), and the predicted vibration spectrum at the pendulum support point (black curve; this is the Z_S input in Fig. 4). Bottom, predicted open-loop fluctuations of the mirror pitch angle (gray curve; the modes at 0.5 and 0.74 Hz are unresolved in this plot), and the residual pitch angle fluctuations when the mirror is controlled by the servo described in Fig. 5 (black curve). The integral of this spectrum equals 8×10^{-9} rad rms.

ment of each interferometer mirror be maintained within 10^{-8} rad rms of optimal, the input beam jitter be below 1.5×10^{-14} rad/ $\sqrt{\text{Hz}}$ (in angle) and 2.8×10^{-10} m/ $\sqrt{\text{Hz}}$ (in transverse displacement) at 100 Hz, and the beam centroids be held within 1 mm of the center of rotation of each of the test masses.

Inasmuch as the angular stability of any local laboratory reference frame on the Earth's surface is inadequate (typically it deviates by perhaps 10^{-7} rad rms on relevant time scales over the 4-km arm length of the LIGO), an automatic alignment system that determines angular errors with respect to the phase fronts of the laser beam itself is indispensable. Using a spatially resolved extension of the RF phase-modulation detection scheme that observes the beating between different transverse spatial modes, we have developed a wave-front sensing scheme for the LIGO that can discriminate all angular degrees of freedom and that can accurately determine the misalignment angles, in principle to much higher accuracy than required. By modeling the detailed physical mechanisms that induce misalignment, we have developed a feedback control design based on these sensors that reduces these fluctuations to the required level without introducing excess sensing noise into the active gravitational wave observation band.

We have presented a comprehensive study of the alignment of an interferometric gravitational wave

antenna. By exploring the underlying mechanisms by which alignment affects interferometer sensitivity, the paths and mechanisms for environmental influence to affect alignment, and the design considerations that are necessary for alignment sensing and feedback control, we have established that LIGO interferometers can be built and operated at the required sensitivity level. We expect that the formalisms and methods introduced here will form an adaptable basis for treatment of alignment control issues for advanced gravitational wave interferometer designs that are now in the planning stages. In addition, the same modal approach can be used to develop sensors for the overlap of cylindrically symmetric modes (mode matching) of the light to the optical system.^{11,17}

Appendix A. Interferometer Parameters

The interferometer parameters used to model the system are given in the list below:

Input test masses (ITM's)	
Power reflectivity	96.995%
Power transmission	3.00%
Radius of curvature	-14,571 m
Diameter/thickness	0.25 m/0.10 m
Index of refraction	1.44968
End test masses (ETM's)	
Power reflectivity	99.9935%
Power transmission	0.0015%
Radius of curvature	7400 m
Diameter/thickness	0.25 m/0.10 m
End test masses (RM's)	
Power reflectivity	97.5%
Power transmission	2.44%
Radius of curvature	9998.33 m
Diameter/thickness	0.25 m/0.10 m
Beam splitter (BS)	
Power reflectivity	49.9625%
Power transmission	49.9625%
Radius of curvature	∞
Diameter/thickness	0.25 m/0.04 m
Arm cavity length (L_1, L_2)	3999.01 m
Recycling cavity ($l_1 + l_2$)/2	9.38 m
Michelson asymmetry ($l_1 - l_2$)	0.210 m
Light wavelength	1.064 μm
Resonant sideband frequency	23.97 MHz
Nonresonant sideband frequency	35.96 MHz

We thank the entire LIGO team at the California Institute of Technology and the Massachusetts Institute of Technology for assistance and support. We especially thank Yaron Hefetz for his contributions at the early stages of this project. This research was supported by National Science Foundation grant PHY-9210038.

References and Notes

1. A. Abramovici, W. E. Althouse, R. W. P. Drever, Y. Gürsel, S. Kawamura, F. J. Raab, D. Shoemaker, L. Sievers, R. E. Spero, K. S. Thorne, R. E. Vogt, R. Weiss, S. E. Whitcomb, and M. E. Zucker, "LIGO: the Laser Interferometer Gravitational-wave Observatory," *Science* **256**, 325-333 (1992).
2. A. Giazotto, "The VIRGO experiment: status of the art," in *First Edoardo Amaldi Conference on Gravitational Wave Experiments*, E. Coccia, G. Pizella, and F. Ronga, eds. (World Scientific, Singapore, 1995), pp. 86-99.
3. K. Danzmann, "GEO 600—600-m laser interferometric gravitational wave antenna," in *First Edoardo Amaldi Conference on Gravitational Wave Experiments*, E. Coccia, G. Pizella, and F. Ronga, eds. (World Scientific, Singapore, 1995), pp. 100-111.
4. K. Tsubono, "300-m laser interferometer gravitational wave detector (TAMA300) in Japan," in *First Edoardo Amaldi Conference on Gravitational Wave Experiments*, E. Coccia, G. Pizella, and F. Ronga, eds. (World Scientific, Singapore, 1995), pp. 112-114.
5. M. E. Gertsenshtein and V. I. Pustovoit, "On the detection of low frequency gravitational waves," *Sov. Phys. JETP* **16**, 433-435 (1963); R. Weiss, "Electromagnetically coupled broadband gravitational antenna," *Mass. Inst. Technol. Res. Lab. Electron. Q. Rep.* **105**, 54-76 (1972).
6. R. Drever, J. Hough, W. Edelstein, J. Pugh, and W. Martin, "A gravity-wave detector using an optical resonator," in *Proceedings of the Ninth International Conference on General Relativity and Gravitation*, E. Schmutzer, ed. (VEB, Berlin, 1980), pp. 265-267.
7. R. W. P. Drever and colleagues, "Gravitational wave detectors using laser interferometers and optical cavities: ideas, principles and prospects," in *Quantum Optics, Experimental Gravity and Measurement Theory*, P. Meystre and M. O. Scully, eds. (Plenum New York, 1983), pp. 503-524; H. Billing, K. Maischberger, A. Ruediger, R. Schilling, L. Schnupp, and W. Winkler, "The Munich gravitational wave detector using laser interferometry," *ibid.*, pp. 525-566.
8. M. W. Regehr, F. J. Raab, and S. E. Whitcomb, "Demonstration of a power-recycled Michelson interferometer with Fabry-Perot arms by frontal modulation," *Appl. Opt.* **20**, 1507-1509 (1995).
9. A. Schenzle, R. DeVoe, and G. Brewer, "Phase-modulation laser spectroscopy," *Phys. Rev. A* **25**, 2606-2621 (1982); R. W. P. Drever, J. L. Hall, F. V. Kowalski, J. Hough, G. M. Ford, A. J. Munley, and H. Ward, "Laser phase and frequency stabilization using an optical resonator," *Appl. Phys. B* **31**, 97-105 (1983).
10. L. Schnupp, Max Planck Institute for Quantum Optics, Garching, Germany (personal communication, 1986).
11. Y. Hefetz, N. Mavalvala, and D. Sigg, "Principles of calculating alignment signals in complex optical interferometers," *J. Opt. Soc. Am. B* **107**, 1597-1605 (1997).
12. L. Schnupp, Max Planck Institute for Quantum Optics, Garching, Germany (personal communication, 1989); T. M. Niebauer, R. Schilling, K. Danzmann, A. Rüdiger, and W. Winkler, "Nonstationary shot noise and its effect on the sensitivity of interferometers," *Phys. Rev. A* **43**, 5022-5029 (1991).
13. The eigenvalue of this mode (u_2) depends somewhat on the quality of the carrier interference at the antisymmetric port because any noninterfering carrier power contributes to the shot-noise level and thus will tend to increase the eigenvalue. However, in these calculations the shot-noise-producing power is always dominated by the sideband power, and for realistic estimates of the carrier contribution the u_2 eigenvalue does not increase by more than 50%. The sideband power dominates because, even though the carrier interference is perfect when there are no misalignments, to better simulate the real interferometer the chosen modulation index is optimal for the expected level of imperfect carrier interference, where of the order of 10^{-3} of the carrier power in the recycling cavity leaks from the antisymmetric port.
14. J. A. Arnaud, "Degenerate optical cavities," *Appl. Opt.* **8**, 189-195 (1969).

15. See G. González and P. Saulson, "Brownian-motion of a mass suspended by an anelastic wire," *J. Acoust. Soc. Am.* **96**, 207–212 (1994); A. Gillespie and F. Raab, "Thermally excited vibrations of the mirrors of laser interferometer gravitational-wave detectors," *Phys. Rev. D* **52**, 577–585 (1995) for thermal noise applied to translational degrees of freedom. The theory can be extended to rotational degrees of freedom.
16. S. Kawamura and M. Zucker, "Mirror-orientation noise in a Fabry–Perot interferometer gravitational wave detector," *Appl. Opt.* **33**, 3912–3918 (1994).
17. E. Morrison, B. J. Meers, D. I. Robertson, and H. Ward, "Experimental demonstration of an automatic alignment system for optical interferometers," *Appl. Opt.* **33**, 5037–5040 (1994); "Automatic alignment of optical interferometers," *Appl. Opt.* **33**, 5041–5049 (1994).
18. J. Giaime, P. Saha, D. Shoemaker, and L. Sievers, "A passive vibration isolation stack for LIGO: design, modeling, and testing," *Rev. Sci. Instrum.* **67**, 208–214 (1996).
19. A. Rohay, "Ambient ground vibration measurements at the Livingston, Louisiana LIGO Site," internal report, LIGO-C961022-A-D (LIGO Document Control Center, California Institute of Technology, 1996).
20. T. Thompson, W. Miller, and E. Ponslet, "LIGO seismic isolation system preliminary design review document," internal report, LIGO-C970251-00-D (LIGO Document Control Center, California Institute of Technology, 1997).
21. N. Mavalvala, D. Sigg, and D. Shoemaker, "Experimental test of an alignment sensing scheme for a gravitational-wave interferometer," (to be published).